4. PARTICIPATION IN THE ASDEX UPGRADE PROGRAMME[1]

M.E. Manso and F. Serra (Heads), R. Galvão, L. Cupido, L. Fattorini, V. Plyusnin, F. Salzedas, P. Varela, I. Nunes, T. Ribeiro, J. Santos, A. Silva, F. Silva D. Borba, R. Coelho, L. Meneses, S. Graça

4.1. INTRODUCTION

The Portuguese participation in the ASDEX Upgrade (AUG) programme has been mainly focused in two research lines:

- Microwave reflectometry;
- MHD, turbulence and transport.

4.2. MICROWAVE REFLECTOMETRY

4.2.1. Microwave system and electronics

The following main activities were made concerning the upgrade of the reflectometry system; the improvement of its operation and reliability and its maintenance:

- Implementation and testing of the heterodyne Q-band fixed frequency channel using synthesizer sources;
- Development of a new routing of the in-vessel waveguides to avoid future PSL induced damage to the waveguides;
- Modification of the in-vessel access of W band oversized waveguides as well as new routing of the oversized W band waveguides outside the vessel to accommodate the shift to the C port access, imposed by the installation of the new ECRH antennas;
- Repair/replacement of parts of transmission line that have been damaged in the last AUG campaign, namely the high-field side Ka band (waveguide and directional coupler) and Q band for X mode operation (waveguides).

4.2.2. Control and data acquisition

4.2.2.1. Main activities

The main tasks performed were:

- Adaptation of the control clients to allow secure remote operation. Due to security/management restrictions, the implementation of a SSL/TLS secure encrypted communication layer on the client and daemon server has been replaced by a different approach. A simple socket tunneling procedure using SSH was implemented, which provides secure access to in-site workstations, allowing remote use of the operation/monitoring clients;
- Implementation of the daemon to control the Fluctuation Monitor System and the respective C/X windows client. The control software of the Fluctuation Monitor System uses a client/server approach, like the broadband system. This software has been completed and is expected to be in advanced test/debug phase in the beginning of 2004 experimental campaign;
- Implementation and test of a Java version dedicated to the Broadband System client;
- Implementation of a Java version dedicated to the Fluctuation Monitor System client (under test).

4.2.2.2. Implementation and test of a Java version dedicated to the Broadband System and Fluctuation Monitor clients

The Java version of the *Broadband System* client and the *Fluctuation Monitor System* client include an UML analysis divided in two parts. The first part corresponds to the communication between daemon and client (Figure 4.1), and the other part to the graphical interface of the client (Figure 4.2).

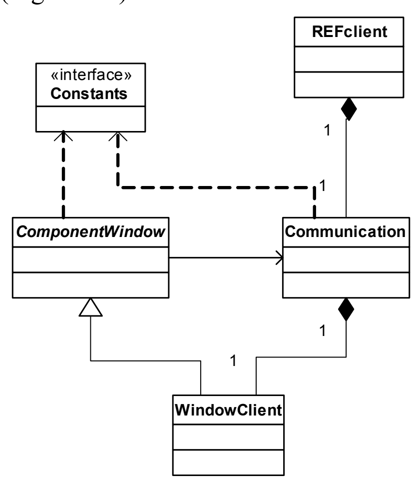

Figure 4.1 - Class Diagram of Communication part

[1] Work carried out in collaboration with the ASDEX-Upgrade Team, of the Association EURATOM/IST. Contact Person: G. Conway.

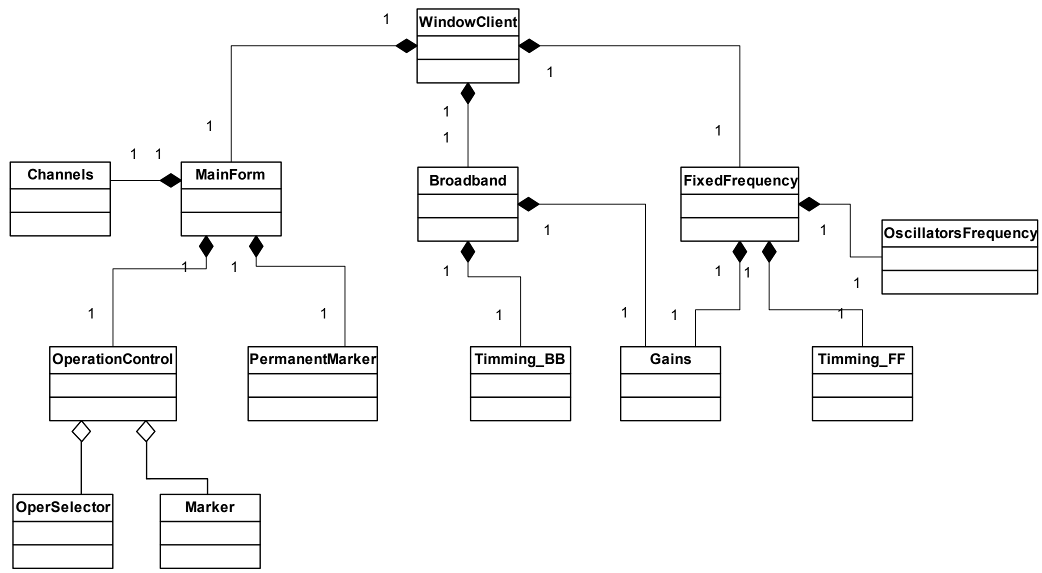

Figure 4.2 - Diagram classes of graphical interface of the Broadband client

Presently, the Java versions of the remote clients are the only ones to implement direct SSH tunneling to connect to the control daemons. They can be used in any operating system with a Java Virtual Machine (vs. 1.2 and higher).

4.2.3. Data Processing

4.2.3.1. Main activities

The following main activities were carried out aiming to improve the accuracy of automatic density profiles, in particular in the presence of high plasma turbulence as well as transient phenomena, such as ELMs:

- Automation of the O-mode density profiles initialization using X-mode data;
- Automatic removal of ELM effects from burst-mode (level-2) profiles;
- Preliminary work concerning the automatic selection of the optimized window length for the spectrogram analysis of reflectometry data.

4.2.3.2. Automatic initialization of O-mode density profiles using X-mode data

A code for the automatic initialization of the density profiles with X-mode data was incorporated into the level-1 data analysis software. The code automatically checks for the availability of X-mode data and uses it to estimate the position of the zero-density plasma layer.

Preliminary analysis of X-mode data (Q and V bands) however indicates that both channels require hardware upgrades before data can be used. The problems are:

- The performance of the Q_X passive doubler is low due to aging and it should be replaced by an active doubler. This upgrade will provide additional power that should improve the signal quality, which is essential for accurate first frequency estimation;
- The radiation pattern exhibited by the V_X antenna is not the more adequate and therefore the antenna should be replaced by a new one as soon as possible.

Due to the above problems the automatic initialization procedure has been disabled in the routine evaluation of the density profiles.

4.2.3.3. Automatic removal of ELM effects from burst-mode profiles

A code for the automatic removal of ELM effects has been incorporated in the level-2 data analysis software, in order to reduce distortions of the burst-mode profile due to ELMs.

The procedure is fully automatic and uses the ASDEX Upgrade ELM diagnostic to identify the time windows where ELMs occurred. All burst profiles acquired in these time windows are removed from the level-2 (RPS) diagnostic.

4.2.3.4. Automatic window length selection for the analysis of reflectometry data using the spectrogram.

Initial work has been done in order to investigate the application of algorithms that would allow the automatic selection of the window length based on the frequency content of the reflectometry signals, rather than the actual procedure made by the user according to a-priory knowledge about the plasma regime, representing normally a compromise between time and frequency resolutions in the spectrogram analysis.

Preliminary results show that the computing overload resulting from this kind of algorithms is acceptable if its application is restricted to the last band processed for each profile. From a physics point-of-view this is also acceptable since it is expected that this band is the one featuring a broader beat-frequency excursion.

This work is now in the test and tuning phases and is expected to enter the level-1 routine evaluation code still during the 2004 ASDEX Upgrade campaign.

4.2.4 Diagnostic developments

4.2.4.1 Main activities

The main activities concerned:

- The development of a software tool to simulate O/X mode reflectometry experiments aiming to improve the accuracy of profile initialization from O mode and to investigate the possibility of measuring $B_t(r)$ with combined O and X mode probing;
- The assessment of the reliability and accuracy of plasma position measurements from reflectometry in typical plasma scenarios using a specially developed workbench of numerical tools.

4.2.4.2 Simulation of O/X mode experiments

Numerical studies were performed showing that the group delay (the relevant information for profile evaluation) obtained with X mode, τ_g^X, is quite sensitive to density gradient variations while the sensitivity to magnetic field changes is much lower (only significant at the very edge plasma). Magnetic field ripples create distortions in the cutoff frequency profile. To reconstruct the density profile from X-mode group delay measurements, using an inversion algorithm, it is necessary to input the magnetic field profile (derived from magnetic diagnostics) and the value of the first fringe f_0, corresponding to the first reflectometry signal reflected from the plasma. Simulations show that the main effect of varying the magnetic field is a radial translation of the density profile while variations of f_0, modify also the profile shape. As f_0 is often difficult to measure accurately, a new technique has been developed for profile reconstruction where the group delay τ_g^O measured from O-mode, is matched to the group delay τ_g^X from X-mode measurement after converted to the corresponding O-mode values $\tau_g^{X\to O}$. Figure 4.3 shows the dependence of the total group delay on the O-mode frequencies. The orange line is the O-mode group delay, starting from 16 GHz, for a reference density profile; while the red line is the X-mode group delay, converted in O-mode also for the reference density profile. There is an overlapping region between 16 and 48 GHz. The blue line is obtained using for the inversion a magnetic field with an error of 0.5%. The green line is obtained using a first fringe frequency 1 GHz more than the reference. Simulations show that the correct values of $\tau_g^{X\to O}$ can be obtained by adjusting both f_0 and the magnetic field profile. Results reveal accurate profile reconstruction with discrepancies of less than 1 mm. Furthermore the technique has the potentiality to provide an estimation of the magnetic field profile.

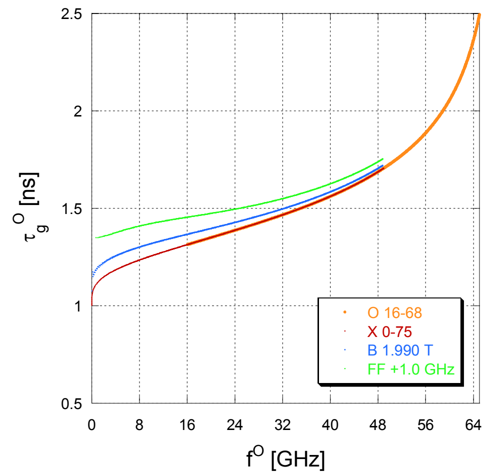

Figure 4.3 – O/X modes group delays matching

4.2.4.3 Integrated tools to simulate profile evaluation

A workbench of integrated tools was developed for the systematic study of experimental and simulated data at all steps of the profile evaluation. These tools, that include a 1D reflectometry simulator adapted to the ASDEX Upgrade geometry, will allow sensitivity studies and the experimentation of new algorithms related to the real time use of reflectometry for plasma position and shape control. The use of neural networks or other techniques will be the main focus of the study to be performed with the workbench tool presently being tested.

4.2.5. Modelling

4.2.5.1. Main activities

The main activities were performed:

- The study of the signature that q=2 type islands produce on the reflectometry signals to investigate the possibility of localizing rational surfaces as a contribution of reflectometry to the estimation of the q-profile;
- The validation of burst-mode analysis used for density profile evaluation with a 2D FDTD full-wave code.

4.2.5.2. Simulation of Amplitude and Phase Variations Induced by Magnetic Islands plus Turbulence

A. 2D FDTD code

Using a Finite Difference Time Domain code (FDTD) it was shown with previous numerical studies, that the magnetic islands may lead to a drop in the amplitude of the detected reflectometry signals due to strong variations in the phase derivative (or group delay), which can be caused by destructive interference. A chain of islands may induce similar effects in the vicinity of the X-points as shown with an Helmholtz code.

To investigate more precisely those effects (including the motion of the islands chain) we used a 2D FDTD code and include density fluctuations with a wavenumber spectrum according to experimental data. To be as close as possible to the experimental settings on tokamaks, we also consider a single island located at the resonant surface $q=2$, whose dimensions are of the same order of magnitude as the phenomena observed on ASDEX Upgrade or Tore Supra.

B. Model for a chain of islands

The chain of islands is modeled by:

$$\delta n_e = A_f \exp\left[\frac{-(x-x_i)^2}{w_x^2}\right]\times \times abs\{\sin\left[N_i k_m (y-y_i(t))+\varphi_i\right]\}, \quad (4.1)$$

where $k_m = 11.6\, rad\cdot m^{-1}$ is the (angular) wave-number corresponding to the width of the calculation box (poloidally), N_i the number of islands in the box at a time, x_i the radial position of the chain, $w_x = 18.75\, m$ determines the radial width of the island, $A_f = 3.5\times10^{18}\, m^{-3}$, the chain is placed radially at $x_{c_{35}} = 31.2\,\lambda_{40GHz}$, the cut-off position for $f = 35\,GHz$ and $\varphi_i = \pi/2$. Parameters were chosen to attain a density plateau of $\approx 7\lambda_{40GHz} = 5.25\,cm$. The chain starts moving poloidally at $t = 500\times T_{40GHz}$ until $t = 2500\times T_{40GHz}$ while being probed with fixed frequency at $f = 38.4\,GHz$. We will henceforth say that the chain is at an X or an O-point when these structure points are aligned with the antenna longitudinal axis.

With one island in the probing wave pattern The detected electric field in the waveguide for one-island chain ($N_i = 1$) the moving structure, with a length of $L_y = 27cm$, induces a reinforcement in the electric field E_z at the X-point where the density cutoff layer acts as a reflector channeling the field into the antenna, strengthening the field amplitude. Destructive interference occurs at the immediate vicinity of the X-point where the return field from frontal reflection interferes destructively with the field reflected from the advancing, larger part of the structure. The field in the wave-guide is effectively highly reduced.

C. Effect of turbulence

With the conditions used above a background of turbulence was added to the plasma. The RMS value of the turbulent fluctuations at $x_{c_{35}}$ was $\delta n_e/n_e = 1.5\%$. With this level of turbulence the island coherent structure starts to distort the pattern that the moving modulated island imposes on the return field (Figure 4.4). A. Multi-reflection effects appear and break the conditions leading to the occurrence of destructive interference and consequently the drops of amplitude start to be smoother.

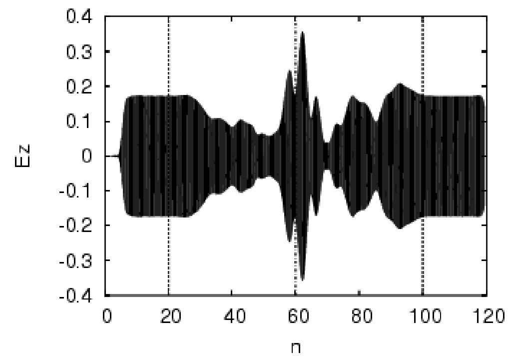

Figure 4.4 - A Reflected signal detected in the waveguide for a moving one-island chain with added turbulence.

D. Simulation of a $q=2$-type island

A structure with magnitude comparable to the islands present on the resonant surfaces q=2 at ASDEX Upgrade or Tore Supra is simulated. To model it we use the expression

$$\delta n_e = -a(x-x_i)\exp\left[-b(x-x_i)^4\right]\times abs\{\sin[N_i k_m (y-y_i(y))+\varphi_i]\} \quad (4.2)$$

where $a = 1\times10^{-7}\, m^{-4}$ and $b = 2.5\times10^{-3}\, m^{-4}$ were chosen to give a pedestal followed by a flat plateau centered around $x_{c_{35}}$. $\varphi_i = \pi/2$. The studies presented in this section were made using swept frequency (FM-CW) in the K_a band. The island is fixed during the sweep. Unlike the case of the small number perturbations, there are no significant modifications at the X-point or in its neighbourhood. Turbulence is added to the plateau with a RMS value at $x_{c_{35}}$ of $\delta n_e/n_e = 1.5\%$. Its effect on the phase derivative $\partial\varphi/\partial f$ show (Figure 4.5) a blurring of the mode signature and the addition of noise after the main mark in $\partial\varphi/\partial f$, which is in agreement with experimental observations. With the same level of turbulence on the whole plasma, we notice that the presence of the mode is once more distorted and noise is added after the main peak in $\partial\varphi/\partial f$.

The simulations show that turbulence distorts the signatures of coherent perturbations, such as MHD imposes on the signal amplitude and phase. For the parameters used in the simulations, a value above 1.5% in the RMS of the fluctuations is enough to produce severe distortion of $\partial\varphi/\partial f$ whereas for 2.5% the mode signature disappears.

Simulations show that larger structures, such as the simulated $q = 2$ island, impose at the O-point, a jump in the phase derivative (time of flight). The X-point does not impose a signature on the phase derivative but presents the possibility of destructive interference close to those surfaces.

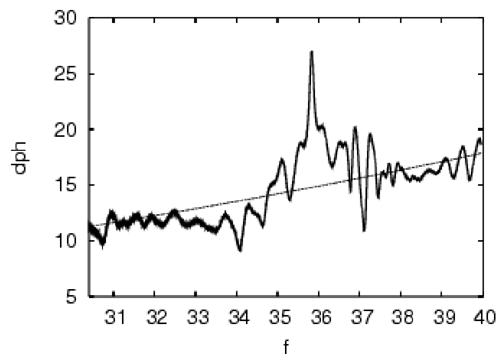

Figure 4.5 - Phase-derivative for frequency sweep, probing a q=2-like island, at the O-point, with turbulence on the whole plasma.

4.2.5.3. Validation of burst-mode analysis using a 2D FDTD full-wave code

A. Burst mode analysis

The burst-mode data processing method was first applied to reflectometry data in ASDEX Upgrade to reduce the distortion of measured density profiles caused by plasma turbulence. The method considers data in bursts of several frequency sweeps taking advantage of the ultra-fast sweeping capability of the diagnostic. A typical setup takes eight closely spaced (10μs) ultra-fast (25μs) sweeps to obtain an *average* profile with a temporal resolution of 270μs. The method uses all the information in the individual spectrograms of the reflectometry signals, enhancing the features common to the sweeps in the burst and strongly reducing the spurious perturbations that might be present in some sweeps due to plasma turbulence. The burst-mode group delay is then obtained from the combined spectrogram using the best-path algorithm .

Figure 4.6 shows the capability of burst-mode analysis to smooth perturbations presented in individual sweep measurements. The burst mode technique applies statistics only to the coherent part of the measurements with the advantage that it does not need any a priori knowledge about this coherence, whereas standard average methods would include also the signal non-coherent parts.

B. Simulations of Profile reconstruction and coherent mode tools

The simulation of data processing used in the experimental signals is important to validate its domain of application. This is the case of data analysis tools used to evaluate the phase derivative for profile reconstruction as well as the limitations introduced in the analysis by density fluctuations.

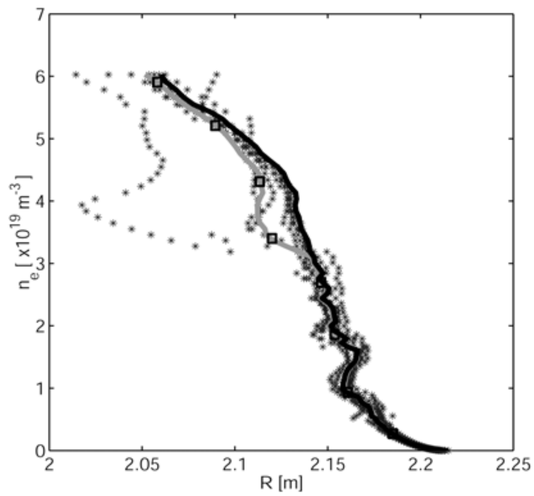

Figure 4.6 - Density profiles obtained with the burst mode (continuous curve), average (gray with squares) and single sweep (asterisk) analysis. The phase derivative perturbations present in some sweeps cause large deviations in both the average and single-sweep profiles. The burst profile, however is not affected.

Simulations were made on a $51\lambda_{40\mathrm{GHz}} \times 36\lambda_{40\mathrm{GHz}}$ grid, probing a linear plasma whose maximum value is $2.5\times10^{19}\,\mathrm{m}^{-3}$ ($f_{\mathrm{pe}} = 45.0\,\mathrm{GHz}$) at $x = 33\,\lambda_{40\mathrm{GHz}}$. The normalized magnitude k-spectrum is constant $(S_{amp} = 1.0)$ for small $k = (k_x^2 + k_y^2)^{1/2}$ satisfying $|k_x|, |k_y| \le 400\,\mathrm{rad\,m}^{-1}$ from where it decays proportionally to k^{-3}.

The frequency is swept probing a density range $[1-2]\times10^{19}\,\mathrm{m}^{-3}$, corresponding to $[30-40\,\mathrm{GHz}]$ frequency band. Since experimental sweeping times are in the order of $20\,\mu\mathrm{s}$, this density fluctuation can be considered frozen. Sweeps are made in groups of 8, each group at a different fluctuation level. We define the fluctuation level in percentage of the ratio between the root mean square (RMS) value of the fluctuation matrix $\delta n_{e_{TRB}}$ and value of the density at the cut-off position for a frequency of $35\,\mathrm{GHz}$ (middle-band) $n_{e-35\mathrm{GHz}}$. Each of the 8-burst runs (frequency sweeps with different fluctuations snapshot), the reflectometry signals is processed using the methods described in Figure 4.6.

In Figure 4.7 the burst mode phase derivatives $\partial\varphi/\partial f$ obtained for several levels of turbulence $\delta n_{e-RMS} / n_{e-35\mathrm{GHz}}$, namely 0.5%, 1.0%, 1.5%, 2.0%, 2.5%, 5.0% and 10.0%, together with the theoretical Wentzel-Kramers-Brillouin (WKB) solution for the unperturbed plasma. Up to 2.5% the burst mode technique soundly recovers the base profile *under the turbulence*. For 5.0%

and 10.0% the obtained phase derivatives detach form the WKB solution.

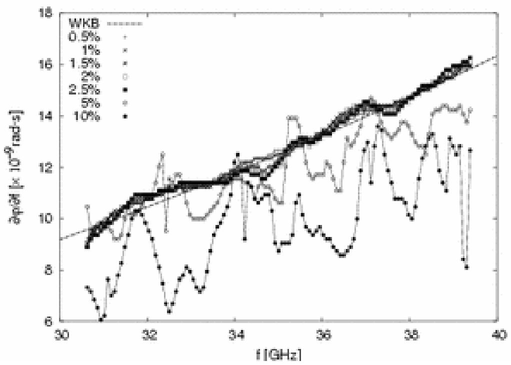

Figure 4.7 - Phase derivatives for several levels of turbulence. The continuous line is the theoretical Wentzel-Kramers-Brillouin (WKB) solution for the unperturbed plasma

In order to evaluate the error bars and to know the behaviour of the burst mode phase derivative, the root mean square error (RMSE)

$$\text{RMSE}=\sqrt{\frac{1}{N-1}\sum_{i=0}^{N-1}\left[\left(\frac{\partial\varphi_{\text{BRST}}}{\partial f}\right)_i-\left(\frac{\partial\varphi_{\text{WKB}}}{\partial f}\right)_i\right]^2} \qquad (4.3)$$

of the burst mode phase derivative $\partial\varphi_{\text{BRST}}/\partial f$ when referenced to the $\partial\varphi_{\text{WKB}}/\partial f$ were computed and presented in Figure 4.8, for several levels of turbulence. Around $\delta n_{e-RMS}/n_{e-35\text{GHz}}$=3.5% there is a change in the evolution of the error, corresponding to a change in the type of response of the system (which goes from linear to non linear), rather than a failure of the analysis method. For a turbulence of 5% the graphic shows also RMSE points obtained for four more burst calculated for independent sets of turbulence matrixes. The statistical dispersion seems to be of the same order of magnitude than the fluctuations observed on the *main set* of samples indicating that the obtained error represent a characteristic of the system rather than a statistical fortuity.

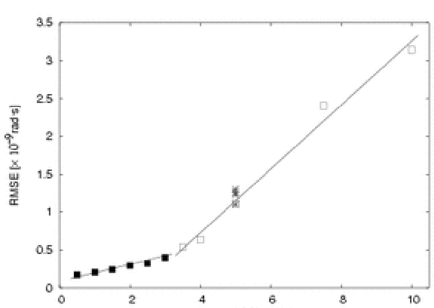

Figure 4.8 - Evolution of the error with the level of turbulence. Around ~3.5% there is a change in the type of response of the system which goes from a linear to a nonlinear behavior.

4.2.6. Plasma physics studies

4.2.6.1 Main activities

The following main studies have been carried out:

- Study of the impact of type I and type III ELMs on the plasma edge density profiles;
- MHD and turbulence studies.

4.2.6.2. Scaling of the pedestal width in ELMy H-modes

An open question for the prediction of the pedestal pressure for ITER is the scaling of the pedestal width. The density pedestal width was determined in ASDEX Upgrade ELMy H-modes using ultra-fast (35 μs) reflectometry measurements of the edge density profiles. The width and gradient of the low field side density profiles were analyzed, and the results compared to the neutral penetration model. For this purpose, a set of experiments were done, where some plasma parameters were varied systematically; input power, density, plasma current and triangularity. The plasma current is scanned for two different plasma shapes; (q scan at fixed B_T) I_p = 0.8 and 1.2 MA, (q_{95} = 4.45, 3.10) for δ_{av} = 0.32 and I_p = 0.6, 0.8 MA (q_{95} = 7.13, 4.97) for δ_{av} = 0.27, where δ_{av} is the average triangularity. For fixed *Ip* = 0.8 MA and *PIN* = 5.2 MW, plasma triangularity is varied, δ_{av} = 0.27, 0.32, 0.44. These results also include a power scan with I_p = 0.8 MA and δ_{av} = 0.32, where the total net power is 2.4, 5.2 and 8.3 MW. The magnetic field is kept constant at 2T in all discharges.

Figure 4.9 shows the density pedestal width Δ_{ne} versus the pedestal density for L- and H-mode discharges. For the ELMy H-mode discharges, Δ_{ne} does not change significantly with the scanned parameters. However, for the ELMy H-mode phase, a broadening of the pedestal width is observed for discharges with high input power (P_{IN} = 8.3 MW). For the L-mode phase, Δ_{ne} increases with density.

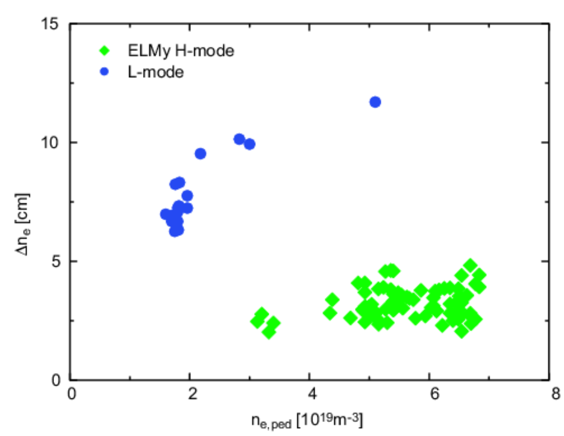

Figure 4.9 - Density pedestal width as a function of $n_{e,ped}$ for ELMy H-mode discharges. This Figure includes also points from density profiles in L-mode.

On the other hand, the density gradient for the ELMy H-mode changes significantly with plasma density (Figure 4.10). Is also found to be proportional to I_p^2 (Figure 4.11), indicating that for the set of data used here, the trigger of the ELMs is related with the ballooning limit.

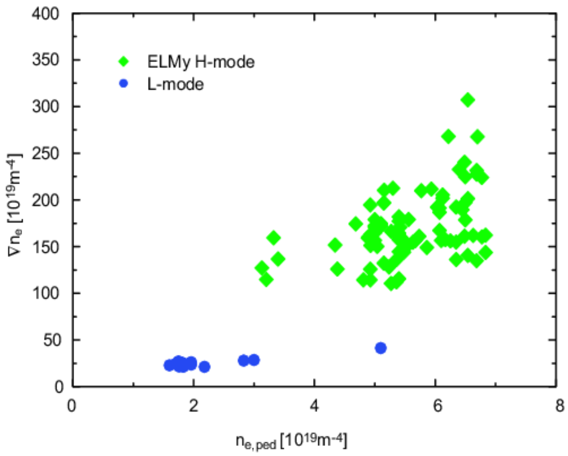

Figure 4.10 - Edge density gradient as a function of $n_{e,ped}$ for ELMy H-mode discharges. This Figure includes also points from density profiles in L-mode.

The pedestal density width measured for this set of discharges is compared against the neutral penetration model. This model predicts that the density pedestal width is proportional to $1/n_{e,ped}$ and the density gradient is proportional to $n_{e,ped}^2$. For the discharges analyzed here, the model holds for the H-mode regime whereas for L-mode regime the pedestal width is observed to increase with density. The pedestal width in L mode is almost three times larger than the corresponding values in the H-mode regime.

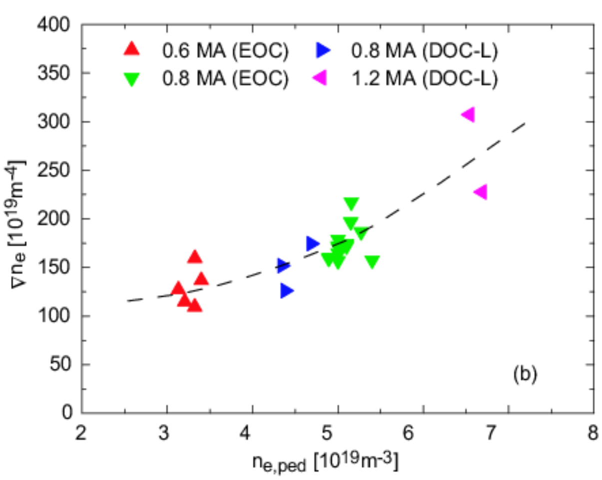

Figure 4.11 - Density pedestal width during a current scan for two different plasma shapes (EOC and DOC-L). It is found that Δ_{ne} stays approximately constant while grad n_e increases with plasma current.

For the density gradient, while in the H-mode regime the density gradient is observed to be ~160×10^{19}m^{-4}, in the L-mode regime this value is around ~50×10^{19}m^{-4}, for the same pedestal density. For this set of ASDEX Upgrade experiments a relation between the experimental results and the model is not observed.

4.2.6.3. ELM particle and energy losses

The dependence on the plasma parameters of the ELM particle and energy losses was studied using the same set of discharges used in the previous analysis.

It is found that the ELM affected depth on the density profiles remains fairly constant with the pedestal density (normalized to the Greenwald limit) up to densities $0.55n_{GW}$ whereas above this value the ELM affected depth is seen to decrease (Figure 4.12).

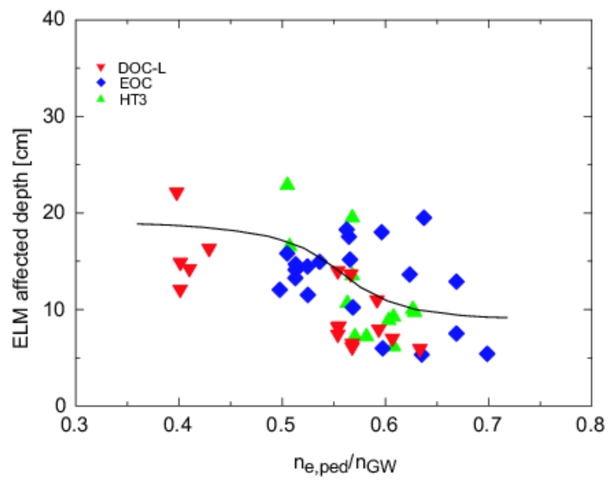

Figure 4.12 - ELM affected depth as a function of the normalized pedestal density, $n_{e,ped}/n_{GW}$ for the LFS. A decrease of the ELM affected depth is observed, for all plasma configurations, for $n_{e,ped}/n_{GW} \geq 0.55$.Line to guide the eye.

There is no clear evidence of the dependence of the ELM affected depth with any of the scanned plasma parameters.

A dependence of the ELM particle losses with the ELM affected depth has been found. Low power discharges have lower ELM particle losses and higher ELM energy losses.

The ELM energy losses has been compared with the four of the existing models ($n_{e,ped}/n_{GW}$, $\nu^*_{(neo)}$, $\tau_{||}$ and f_{ELM}/τ_E for a restricted set of data: density scan for three different triangularities (Figure 4.13). For all four models it is observed that the ELM energy losses decrease with density. When comparing the triangularity dependence, no clear trend is seen, although smaller values of $\Delta W_{ELM}/W_{ped}$ are obtained for the discharges with higher triangularity. Contrary to what is obtained for the ELM

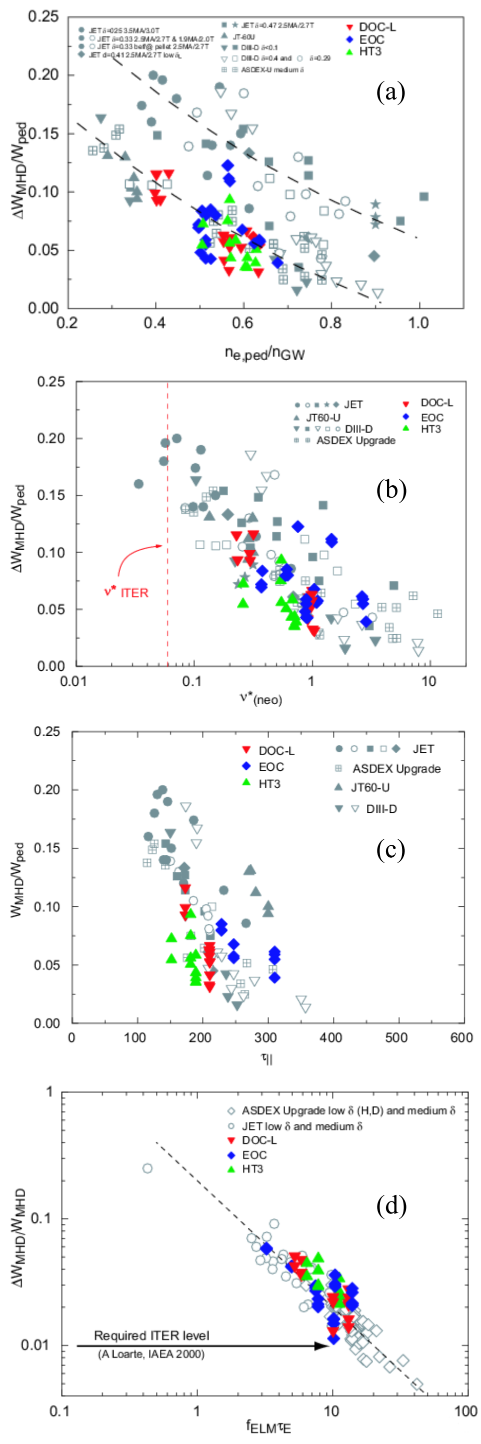

Figure 4.13 - Normalized energy loss ($\Delta W_{ELM}/W_{ped}$) as a function of the (a) pedestal density normalized to the Greenwald limit ($n_{e,ped}/n_{GW}$) (b) the neoclassical collisionality (c) the SOL ion flow parallel time calculated for the pedestal parameters (τ_{ped}) (d) normalized ELM energy loss ($\Delta W_{ELM}/W_{MHD}$) versus the ELM frequency times the energy confinement time ($f_{ELM}\tau_E$), for a large range of plasma parameters and several different devices (in grey) while the points for the discharges being studied here are plotted in colour.

particle losses, the ELM energy losses do not show a clear dependence on the ELM affected depth, indicating a dependence on the pedestal parameters before the ELM, whereas the ELM particle losses show evidence of very weak dependence on the plasma parameters.

The trends observed in this study for the different experiments are very similar for all the scalings shown here. The important difference of these scalings, particularly the ones for the ELM energy reaching the divertor plates lays on the fact of how different the expected ELM energy losses are when an extrapolation for ITER is made. If we take the scaling proposed by Herrmann the expected heat flux reaching the divertor is about one order of magnitude higher than the calculated limit for the ITER divertor, with the present knowledge of possible materials. The same is obtained with the model proposed by Loarte *et al.* based on collisionality. However, another model by Loarte *et al.* predicts that the heat flux is well within the values for present experiments, and consequently the ELMy H-mode regime does not present a problem to the ITER divertor.

4.2.6.4. H-mode transport barrier

The results obtained in this systematic study helped to clarify some aspects of the type I ELM instability for this set of experiments, such as the density pedestal width and gradient. It has been seen that the density pedestal width varies slightly with the density and does not show any dependence with the other plasma parameters scanned. The comparison of the results presented here with the neutral penetration model show that the model does not apply to the obtained data and therefore transport may be a very important factor on the determination of the H-mode transport barrier. This gives an optimistic outlook for the pedestal width of ITER, since high pedestal pressures are required for good confinement. The expected neutral penetration in ITER is rather small (~mm) given rise to very narrow pedestals.

However, it is not clear if the formation of the H-mode transport barrier is dominated by neutral penetration or by transport and more experiments and modelling are needed.

As for the density gradient, it is found that these results are consistent with the ballooning limit indicating that the ELM may be a ballooning instability. More evidence of the ballooning character is observed when comparing the crash of the density profiles at the HFS with the LFS during an ELM event. A delay in the crash of the density profile at the HFS (compared to the LFS) is observed. This delay is of the order of the ion parallel transport time, allowing a physics picture of a mode starting at the LFS and propagating to the HFS.

Another important point related to the operation of ITER in the ELMy H-mode regime, is the ELM size and its influence on the divertor lifetime. What influences the ELM size is then a crucial question. Although no conclusion of which are the plasma parameters that control the ELM size is yet possible, it has been seen that the ELM size depends on the pedestal parameters before the ELM event. The uncertainties in the determination of the pedestal energy and ELM energy losses do not allow at this stage to distinguish between models and further studies are needed.

4.3. MHD AND TURBULENCE STUDIES

4.3.1. Main activities

The main activities performed concerned:

- The computation of turbulence in the scrape-off layer (SOL) region of a tokamak plasma using fluxtube codes, such as DALF or GEM ;
- The study of Alfvén instabilities aiming to contribute to the optimisation of the design and future operation of a fusion tokamak reactor.

4.3.2. Code development for the analysis of turbulence and transport in the SOL of ASDEX Upgrade

In the scrape-off layer (SOL) region of a tokamak plasma, the magnetic field lines are open and strongly deformed due to the proximity of the separatrix, as opposed to the closed field lines region. The equations of the models behind the referred codes have several operators which are geometry dependent, namely, the ExB advection $\partial/\partial t+v_E\cdot\nabla$, the perpendicular Laplacian $\nabla^2_\perp$, the parallel gradients $\nabla_\parallel$ and divergences $B\nabla_\parallel(1/B)$ and the magnetic divergence terms. $K=-\nabla\cdot[(c/B^2)B\times\nabla]$ For this reason, the geometry has influence in the dynamics of turbulence.

The geometry itself is established by the equilibrium magnetic field present in the plasma, which is obtained by solving the Grad-Shafranov equation, a consequence of scalar pressure equilibrium $J\times B=c\nabla p$. A nested set of surfaces (2tori) is assumed, forming an axisymmetric geometrical system for which there is a natural choice of coordinates. These are a radial flux label coordinate (by definition constant within a given surface) and two angular coordinates corresponding to the poloidal and toroidal directions. On this general coordinate system we impose a set of convenient properties that will ultimately define the coordinates themselves, in this case, Hamada coordinates.

$$\Psi \ - \ \text{magnetic poloidal flux}$$

$$\theta = \chi' \int_0^\eta \frac{d\eta'}{\mathbf{B}\cdot\nabla\eta'} \qquad \text{where} \qquad \chi' = \left(\oint \frac{d\eta}{\mathbf{B}\cdot\nabla\eta}\right)^{-1}$$

$$\zeta = \frac{\phi}{2\pi} + \frac{I(\Psi)}{2\pi}\int_0^\eta \frac{d\eta'}{\mathbf{B}\cdot\nabla\eta'}\left(\left\langle\frac{1}{R^2}\right\rangle - \frac{1}{R^2}\right) \tag{4.4}$$

Using similar methods to those behind the construction of the globally consistent flux tube formulation in the referred codes, a fluxtube (modified) Hamada coordinate system was constructed.

To calculate numerically such coordinate system, a code was written, which reads the magnetic field configurations provided by equilibrium codes, such as HELENA, or CLISTE together the gridding code CARRE. Using bicubic splines interpolation and 10point Gauss-Legendre quadrature integration , the Hamada integrals were calculated and all the subsequent coordinates transformations, necessary to obtain the (x, y, s) fluxtube metric coefficients, were performed. With these quantities calculated, all the geometrical information needed for the turbulence model mentioned in the beginning is available, namely, the seven geometrical quantities g^{xx}, g^{xy}, g^{yy}, B^2, b^s, K^x and K^y, all dependent only on the parallel s coordinate. Figures 4.15 and 4.16 show results of the calculation of such quantities for two magnetic field configurations of the tokamak ASDEX Upgrade.

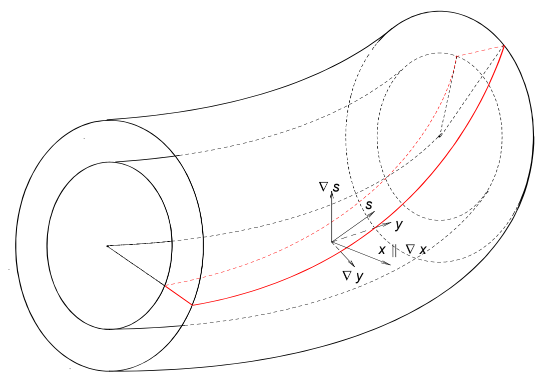

Figure 4.14 - Threedimensional representation of the field aligned fluxtube (Hamada) coordinates and their gradients.

The first case (figure 4.15) shows the closed field line region, on a X-point free magnetic field, obtained from the HELENA code. The shifted metric , a procedure used to address grid cells deformation caused by the non--orthogonality of the coordinates, was applied so that we show $\alpha'_k = (g^{xy}/g^{xx})|_{s=s_k}$ instead of g^{xy}.

The second case (figure 4.16) corresponds to the SOL region. This time, the geometrical information was calculated from an equilibrium outside the magnetic separatrix, provided by the CLISTE code. Note that now the origin in θ corresponds to the top of the tokamak. This must be taken into account when comparing with the previous figure, where the θ's origin corresponds to the outboard midplane.

In terms of the influence of these quantities on the turbulence, $B^2(s)$ gives the variation of ρ^2_s (drift scale) with θ, important as it controls the polarization drift dynamics. The variation of g^{xy} with same coordinate, gives the local shear, calculated by $\partial\alpha_k/\partial s_k$. The effect of the Shafranov shift is felt through g^{xx}, which, in the SOL case presented, shows a clear maximum corresponding to the rightmost side of the plasma in the figure where the flux surfaces are radially compressed. The terms K^μ define the structure of the curvature effect and, finally, b^s plays a role in $\nabla.b=B.\nabla(1/B)$, a flux expansion in the parallel dynamics.

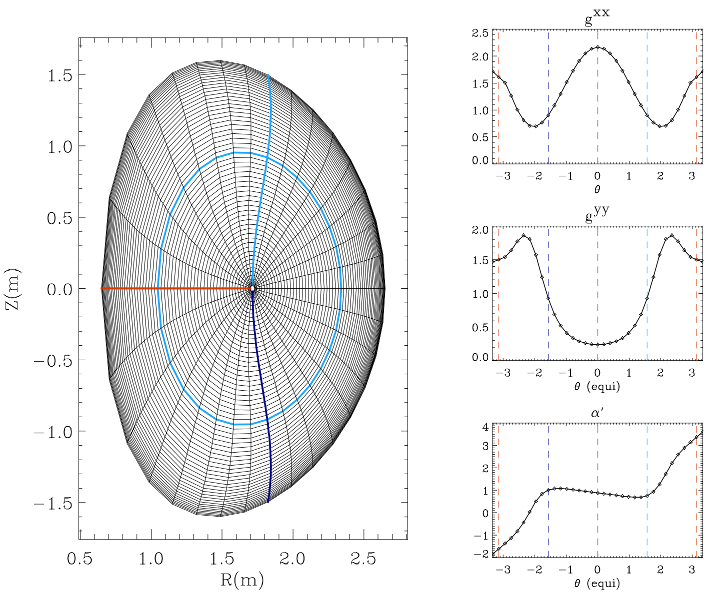

Figure 4.15 - Flux tube shifted metric geometrical quantities (normalised [1]) necessary for the turbulence simulations (right), evaluated on the reference flux surface (blue) shown on the left hand side figure. There, the corresponding magnetic field configuration of ASDEX Upgrade is depicted, as well as the grid calculated (equidistant in θ) for the geometry construction. The branch cut in θ (red line) was made in the inboard midplane.

When comparing the results from these two cases, the differences are clear, and two of them are worth commenting here. The first is that in the X-point magnetic field, the metric components corresponding to the perpendicular directions, g^{xx} and g^{yy}, reveal stronger variations. This has a big impact on the resolution requirements for perpendicular plane grid in the turbulence code. For this reason, GEM (gyrofluid) is the one to be used in SOL simulation, since it can treat space scales below the ion gyroradius. The second difference is the non-periodicity (in s) showed by the second case. This happens because, in the SOL, the field lines end on plates, breaking the field line connection property of the closed flux surfaces. This implies a change in the parallel boundary conditions.

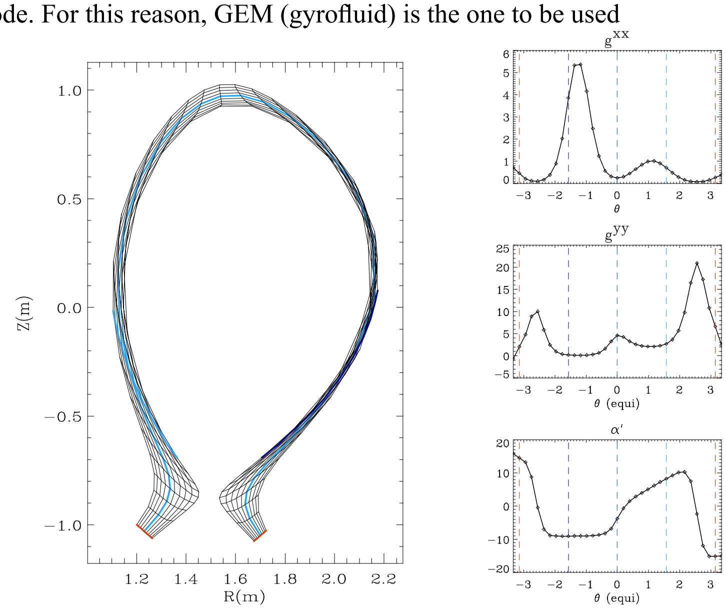

Figure 4.16 - Same as figure 2 but for the SOL region of an X-point magnetic field configuration. Note that now the origin in θ is now on the top of the tokamak, such that -π and π correspond to the outboard and inboard divertor plates, respectively (red lines).

The new boundary conditions, for the SOL region, are obtained by proving the flux variables of the model at the plates (parallel ion velocity, current and heat fluxes). A simple model, based on Debye sheath physics , can be used to yield the particles and energy fluxes to the divertor plates, which provide those conditions. From the first ones he parallel ion velocity and current are obtained:

$$n_{se}u_{Debye} = c_s\left(\frac{\tilde{n_{se}}}{n_{se}} + \frac{1}{2}\frac{\tilde{T}_e}{T_e}\right) \quad \text{and} \quad T_e u_{Debye} = \frac{3}{2}\frac{\tilde{T}_e}{T_e}$$

$$J_{Debye} = en_{se}c_s\left(\frac{e\tilde{\phi}}{T_e} - \Lambda\frac{\tilde{T}_e}{T_e}\right) \tag{4.5}$$

and from the second ones we get the electron and ion heat fluxes

$$q^D_{e\|} = (2+\Lambda)\, n_{se}T_e c_s\left(\frac{\tilde{n}_{se}}{n_{se}} + \frac{3}{2}\frac{\tilde{T}_e}{T_e}\right) \approx 5.5 T_e c_s\left(\frac{\tilde{n}_{se}}{n_{se}} + \frac{3}{2}\frac{\tilde{T}_e}{T_e}\right)$$

$$q^D_{i\|} = \left(3\tau_i + \frac{1}{2}\right) n_{se}T_e c_s\left(\frac{\tilde{n}_{se}}{n_{se}} + \frac{3}{2}\frac{\tilde{T}_e}{T_e}\right) \tag{4.6}$$

where $\Lambda = \log\sqrt{M_i/2\pi m_e}$ and $T_i = \tau_i T_e$.

The geometry and the parallel boundary conditions briefly described here provide what is necessary to perform turbulence computations in the SOL, which constitutes the next step in the work. It will involve the comparison between the turbulence on closed and open flux surfaces, as well as the study of the effect of a realistic SOL geometry. More realistic models for the Debye sheath boundary conditions, including such phenomena as neutral recycling or electron secondary emission, are also planned.

4.3.3. Toroidicity induced Alfvén Eigenmodes (TAE) in ASDEX Upgrade

4.3.3.1 Introduction

Plasma instabilities are of great importance for the optimisation of the design and future operation of a fusion tokamak reactor. Alfvén instabilities are particularly important due to the fact that the charged fusion products (α particles) which provide the plasma heating have a birth velocity v_α=1.3x10^{7}ms^{-1}, larger than the Alfvén velocity $v_A=B/\sqrt{\rho}\approx 10^7$ms^{-1}. Toroidicity induced Alfvén Eigenmodes (TAE) are destabilised in ASDEX Upgrade using Ion Cyclotron Resonant Heating (ICRH). Unstable TAE are observed in the magnetic probes, reflectometer and soft X-rays cameras when the ICRH power exceeds P_{ICRH} > 2.5 MW in both conventional and advanced scenarios. The most unstable TAE have toroidal mode numbers (n=3,4,5,6) and experiments with reversed current and magnetic field showed that the TAE propagate in the current direction, i.e. the ion diamagnetic drift direction, confirming that these modes are destabilised by the ICRH produced energetic ions. The characterisation of the TAE instability in ASDEX Upgrade is reported, focussing on the identification of the toroidal, poloidal and radial mode structure. The data is compared with the ideal MHD model.

4.3.3.2. TAE Amplitude and stability threshold

The most suitable diagnostic for the detection and identification of TAE are the magnetic probes. TAE are in general global modes, which extend towards the plasma edge and can be detected in the vacuum using magnetic sensors. Low amplitude intermittent TAE were observed in the magnetic probes measuring the vacuum magnetic field perturbations, when the ICRH power exceeds P_{ICRH}>2.5 MW at low density (n_e=2-3x10^{19}m^{-3}). TAE with amplitudes larger than $\delta B/dt$>0.08 T/s are clearly seen in the signals, which correspond to vacuum field perturbations of $\delta B/B$ > 2x10^{-7}. By increasing the ICRH power, a larger numbers of modes are observed simultaneously. At the maximum ICRH power obtained in these experiments P_{ICRH}~5 MW, 6 TAE are observed simultaneously. The highest amplitude perturbations measured in the magnetic probes are of the order of $\delta B/dt$=3-4 T/s, which corresponds to vacuum field perturbations of δB=0.025mT or $\delta B/B\sim 10^{-5}$. However, the TAE amplitude is strongly modulated by the occurrence of other plasma instabilities, such as the sawtooth and edge localised modes (ELMs). In the case of the sawtooth, it is known that the crashes remove the fast particles from the core, therefore, removing the drive for the TAE. This explains the strong reduction of the TAE amplitude after each sawtooth crash. On the other hand, the amplitude increases after each ELM collapse. This could be due to the change in the propagation of the TAE in the plasma edge, when the edge plasma parameters are strongly affected by the ELM or due to a change in the distribution function of the fast particles reinforcing the TAE drive.

4.3.3.3. Frequency of the TAE instability

The TAE frequency in the plasma frame of reference is obtained from the measured frequency in the laboratory frame of reference using the Doppler correction given by the plasma toroidal rotation f_{ROT} and the TAE toroidal mode number (n), $f_{LAB}=f_{TAE}+n\ f_{ROT}$. This simple relation is able to explain the frequency splitting between the different TAE toroidal harmonics observed in JET and DIII-D. In both cases, $\Delta f_{TAE=}(f_{TAE\ (n)}-f_{TAE\ (n-1)})$ is largely independent of n. After subtracting the Doppler shift $f_0=f_{TAE}$ - n Δf_{TAE}, all frequencies nearly coincide and f_0 can be inferred as the TAE mode frequency in the plasma rest frame. In the DIIID case, ΔF_{TAE} is comparable to the bulk plasma toroidal rotation measured using spectroscopy. In the JET case, Δf_{TAE} is comparable to the rotation of the n=1 sawtooth precursor, which is also closely link to the bulk plasma toroidal rotation.

In ASDEX upgrade, Δf_{TAE} is also largely independent of n and when the Doppler shift is subtracted $f_0=f_{TAE}$ - n Δf_{TAE} all frequencies also nearly coincide. The resulting frequency (f_0) is comparable with the TAE gap frequency $f_A=V_A/2qR_0$. However, in contrast with the results discussed above from JET and DIII-D, the differences between the frequency of two adjacent toroidal mode numbers $\Delta f_{TAE=}(f_{TAE\ (n)}+f_{TAE\ (n-1)})$ >10kHz cannot be explained solely by toroidal plasma rotation, which is less than f_{ROT}<2 kHz (V_{ROT}<20 km/s) for ICRH only heated plasmas.

4.3.3.4. Toroidal mode number analysis

The analysis of the toroidal mode number (n) is particularly important, since the TAE destabilisation is linked to the breaking of toroidal symmetry by the wave fields in the interaction with the energetic ions. The most unstable toroidal mode numbers are given by the balance between the instability drive proportional to n, which saturates for large n due to finite orbit widths effects, and the various damping mechanisms. Due to toroidal symmetry of the tokamak plasma and weak non-linear coupling between different toroidal harmonics, the TAE have well defined toroidal mode numbers.

The toroidal mode number of the TAE perturbation can be calculated using the magnetic fluctuation measurements from 'Mirnov' sensors located at different toroidal positions. These measurements are sensitive to phase offsets in the signal amplification hardware. Therefore, an appropriate calibration of the signal responses around the TAE frequency need to be carried out before accurate TAE toroidal mode numbers are obtained using the toroidal array of magnetic probes. After the appropriate calibration, the TAE toroidal mode number can be calculated very accurately, even for TAE with low measured amplitudes $\delta B/B \sim 2 \times 10^{-7}$. TAE toroidal mode number for discharges with forward and reversed current and toroidal magnetic field are shown in Figures 4.17 and 4.18 respectively. The convention is that positive toroidal mode numbers signifies propagation in the counter clockwise direction, as viewed from the top of the machine. This is the normal direction of the current in ASDEX Upgrade. Therefore, with the normal current (counter clockwise direction) #16161, the TAE modes propagate in the same direction (positive mode numbers), i.e. the ion diamagnetic drift direction. With reversed current (clockwise direction) #17677, the TAE modes propagate in the opposite direction (negative mode numbers), but again the ion diamagnetic drift direction. This is consistent with the fact that TAE are destabilised by the ICRH produced energetic ions, extracting the free energy from the radial gradients of the fast particle distribution function.

In discharge #16161, a n=-1 is also observed, which propagates in the opposite direction to the other 5 modes (n=1,3,4,5,6) as seen in Figure 4.17. The observed amplitude of the n=-1 and n=1 modes is around δB~0.1 T/s an order of magnitude smaller than the n=3,4,5 modes which is around δB~1 T/s. TAE modes propagating in the direction opposite to the ion diamagnetic drift direction are seen in ASDEX Upgrade, if the ICRH power exceeds PICRH>5MW in conventional scenarios. It is possible that at these levels of ICRH power, particle with large energy and orbit widths are generated. Large orbits leads to non-standard distribution functions and TAE propagating in both directions can be destabilised.

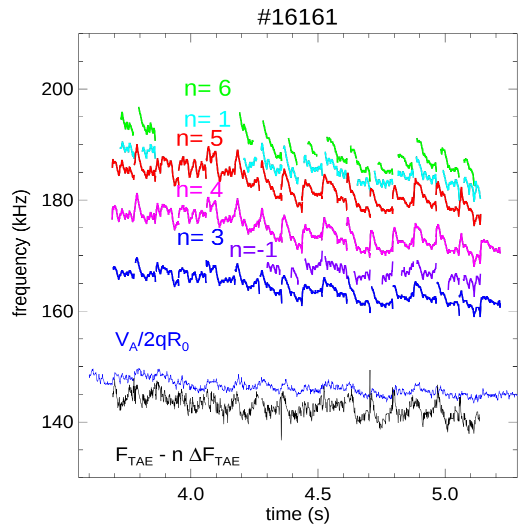

Figure 4.17 - Frequency of the TAE modes observed with different toroidal mode numbers as a function of time, compared with $f_0=f_{TAE}$-n $(f_{(n)}+f_{(n-1)})$ for n=4 and the Alfvén frequency at q=1.5.

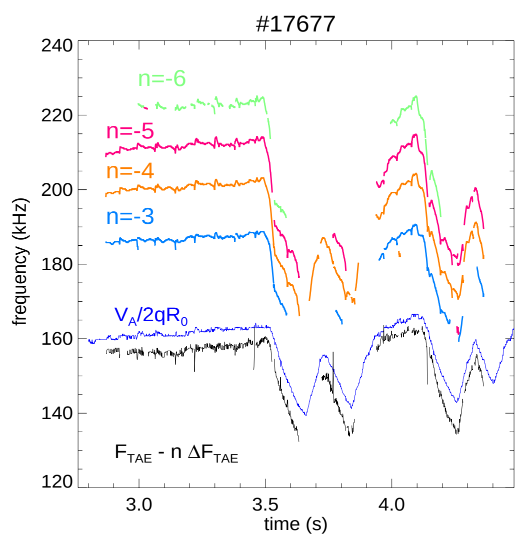

Figure 4.18 - Frequency of the TAE modes observed with different toroidal mode numbers as a function of time, compared with $f_0=f_{TAE}$-n $(f_{(n)}+f_{(n-1)})$ for n=4 and the Alfvén frequency at q=1.5.

4.3.3.5. Poloidal mode number analysis

The poloidal mode structure of the TAE is more complex, because the TAE are created by toroidal coupling of two adjacent poloidal harmonics. Toroidal coupling across the plasma radius generates higher harmonics towards the plasma edge resulting, in a rather different poloidal structure compared with the structure at the rational surface where the mode is generated. Different poloidal harmonics behave differently while propagating in the vacuum, with the higher mode numbers decaying very rapidly. The poloidal wave number measured is largely independent of the toroidal mode number. However, the wave number changes sign, i.e. propagation in the poloidal plane changes direction, when the current and field are reversed. When, TAE propagating in both toroidal directions are destabilised in the same discharge, the poloidal wave numbers also change sign. This result confirms that all modes have the same helicity, consistent with the magnetic field configuration.

4.3.3.6. Radial mode structure

In ASDEX Upgrade, the radial extent of the TAE eigenfunction can be obtained by combining the information from magnetic sensors “Mirnov probes”, microwave reflectometer and soft X-rays emission. The magnetic data provides information on the vacuum magnetic field perturbation outside the plasma. The reflectometer gives information on the perturbation in several radial positions, corresponding to the fixed frequency microwave beam cut-off layers. For the discharges used in these experiments, 4 channels were available on the high field side and 4 channels on the low field side. However, due to the limitation of the homodyne detection system used in these channels, only qualitative amplitude information could be obtained. Therefore, most information is obtained from the horizontal soft x-rays camera C, the only camera installed with fast diodes capable of detecting the high frequency TAE perturbations. Camera C is installed in the outer mid-plane (low-field side), with horizontal lines of sight. Measurements of the soft x-rays emission provides line integrated information on the plasma perturbations caused by the instabilities. The TAE eigenfunction is expected to have a short radial wavelength, especially in the high shear region at the edge, beyond the resolution of the soft x-rays cameras. However, preliminary information on the main features of the eigenfunctions can be obtained using the present diagnostic setup. In the discharge analysed in detail (#17806), the measured TAE amplitude for channels 18-24 in the core region is $\delta\Gamma$=10-40W/m^2, significantly larger than the background fluctuation level, which is around $\delta\Gamma$=5W/m^2. A detailed comparison between the camera C soft x-rays emissivity fluctuation profile and the modelled TAE perturbation calculated using the MISHKA code was performed. The measured emissivity fluctuations $\delta\Gamma$ can be related to the local MHD fluctuations by integrating along the lines of sight. MHD model shows the existence of two n=3 TAE modes in this plasma configuration with distinct radial mode structures: the usual global n=3 TAE, which crosses several continuum gaps and the core localised n=3 TAE, located in a single continuum gap. Comparison between the global eigenfunction and the measured soft x-rays emissivity fluctuations profile, represented in Figure 3, shows good agreement for all channels 16-30. Therefore, it can be concluded that the modes observed are global TAE. The maximum amplitude of the perturbation in the region covered by the soft x-rays camera is 0.39mm, corresponding to a magnetic perturbation of $\delta B/B=10^{-4}$ in the plasma core.

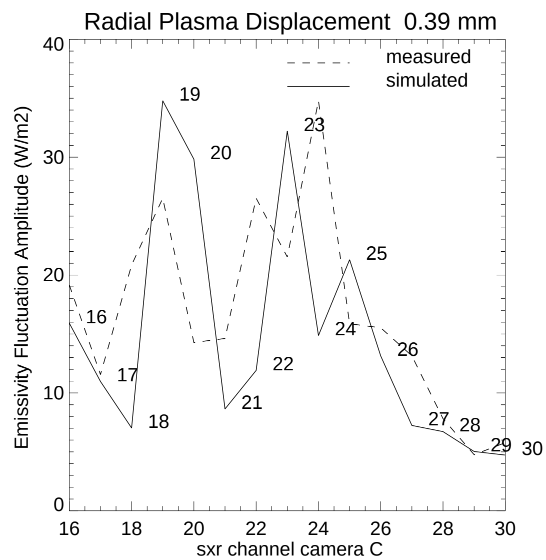

Figure 4.19 - The comparison between the global n=3 TAE eigenfunction and the measured soft x-rays emissivity fluctuations. The maximum amplitude of the perturbation in the region covered by the soft x-rays camera is 0.39 mm.

4.4. OTHER ACTIVITIES

Two members of the IST/CFN staff have participate in the management of the AUG project:

- Prof. Maria Emilia Manso is a member of the AUG Programme Committee;
- Dr. Duarte Borba is the Task Force Leader for TF V (MHD).